

Parity and Time-Reversal Breaking Effects on Resonant X-Ray Scattering at the Fe Pre-K-Edge in Magnetite

Jun-ichi IGARASHI* and Tatsuya NAGAO¹

Faculty of Science, Ibaraki University, Mito, Ibaraki 310-8512

¹*Faculty of Engineering, Gunma University, Kiryu, Gunma 376-8515*

We study noncentrosymmetric effects on resonant x-ray scattering (RXS) in magnetite. The noncentrosymmetry at A sites in spinel structure makes the $4p$ states strongly hybridize with the $3d$ states through neighboring oxygen $2p$ states, giving rise to the non-vanishing contribution of the dipole-quadrupole ($E1-E2$) process in the RXS spectra. We substantiate this observation by introducing a microscopic model of a FeO_4 cluster with multiplets and the $4p$ band. We show that the hybridization changes its sign between two kinds of A sites and accordingly the local amplitude from the $E1-E2$ process changes its sign, resulting in non-vanishing RXS intensities at forbidden spots (002) and (006) in the pre-edge region in agreement with the experiment. A large dependence of the pre-edge intensity on the direction of the applied magnetic field is predicted as a consequence of breaking both centrosymmetry and time-reversal symmetry. Furthermore we analyze the intensity difference between two opposite directions of the applied magnetic field at the allowed spot (222) in connection with the experiment. We obtain the intensity difference of a “dispersion” form, which resembles the observed spectra at the Mn pre- K -edge in MnCr_2O_4 but is quite different from the observed one in magnetite. Although the observed spectra are claimed to arise from “magnetoelectric” amplitude, we argue that this claim has no ground.

KEYWORDS: resonant x-ray scattering, magnetite, local noncentrosymmetry, E1-E2 transition, magnetoelectric effect, XMCD, MnCr_2O_4

1. Introduction

Resonant x-ray scattering (RXS) has been widely used to investigate different kinds of orders, such as charge, magnetic and orbital orders in crystals,¹⁻⁵ since the strong resonance makes the signal sensitive to the ordered structure. The K -edge resonance is usually used in transition metals in order to observe signals at superlattice spots associated with the order parameter. This is because the corresponding x-ray wavelength matches the period of long range orders, which is usually an order of atomic distance except for the case of long period.

The RXS amplitude is given by a sum of atomic amplitudes with appropriate phases. Each atomic amplitude is described by a second order process. One of the most dominant processes in transition-metal compounds is the dipole-dipole ($E1-E1$) process that the $1s$

*E-mail:jigarash.mx.ibaraki.ac.jp

electron is excited to the $4p$ states by absorbing x-ray and then the $4p$ electron is recombined with the $1s$ -core hole by emitting x-ray. Since the $4p$ states are extended in space, they are easily influenced by the electronic structure at neighbors to the core-hole site; the $4p$ states are modulated by the lattice distortion through the hybridization to neighboring oxygens, giving rise to the signal at superlattice spots. Therefore, the RXS signal at the superlattice spots arises from the variation of the $4p$ states in accordance with the long-range order, and provides an indirect proof of the order which is usually constructed by $3d$ states. Such a view has been confirmed by theoretical analyses⁶⁻⁸ in connection with the RXS experiment for LaMnO_3 .³

There appear sometimes extra signals with energy below the K -edge, called the pre-edge signals, which will be mainly discussed in the present paper. Since the pre-edge energy is close to the energy exciting an electron from the $1s$ state to the $3d$ states, the signal could be naturally interpreted as arising from the quadrupole-quadrupole ($E2-E2$) process in which the $1s$ electron is excited to the $3d$ states by absorbing x-ray and then one of $3d$ electrons is combined with the core hole by emitting x-ray. However, the pre-edge signal could also be generated from the $E1-E1$ process, since the p -symmetric states with respect to the core-hole site can be constructed from $3d$ states at neighboring transition-metal atoms.^{6,9} These two origins may be distinguished by different peak positions, that is, the peak in the $E2-E2$ process is expected to be located at the region around several eVs lower than that in the $E1-E1$ process, since the relevant $3d$ states in the $E2-E2$ process is on the core-hole site, and is strongly attracted by the core-hole potential.

The situation may become quite different when the centrosymmetry is locally broken. In such circumstances, the $4p$ states could hybridize with the $3d$ states on the same site through the hybridization to neighboring oxygen $2p$ states, and thereby the dipole-quadrupole ($E1-E2$) process could contribute to the pre-edge signals. Such a presence of the $E1-E2$ process has been recognized by the experiment of K_2CrO_4 ¹⁰ and by the numerical calculation for Ge.¹¹ It has been much debated for V_2O_3 .¹²⁻¹⁵ Furthermore, for magnetic materials, the atomic amplitude of the $E1-E2$ process could depend on the direction of the local magnetic moment due to the spin-orbit interaction (SOI), and thereby the pre-edge signals could depend on the direction of magnetic moment. Since the direction of magnetic moment could be controlled by applying the external magnetic field, we could observe such a dependence by changing the external magnetic field. Actually, such signals have been observed¹⁶ and analyzed in a multiferroic system GaFeO_3 ,^{17,18} and also have been discussed in other situations.^{19,20}

The pre-edge signals have also been observed in magnetite, Fe_3O_4 , at forbidden spots of scattering vectors (002) and (006).^{21,22} In addition, the intensity difference with changing direction of the external magnetic field has been measured at spots (222), (333) and (444).^{23,24} The purpose of this paper is to analyze the pre-edge signals in magnetite through a quantitative

calculation of the spectra and to elucidate the mechanism from a microscopic viewpoint.

The magnetite is the first magnetic material known to the mankind. Its crystal structure is the inverse spinel, consisting of iron sites tetrahedrally surrounded by four oxygens (A sites) and those surrounded octahedrally by six oxygens (B sites), as shown in Fig. 1. Since the centrosymmetry is locally broken at the tetrahedral sites, those pre-edge signals are thought to be related to breaking both centrosymmetry and time-reversal symmetry. Analyses based on the microscopic electronic structure, however, have not been worked out yet. We construct a definite model that the $4p$ states form an energy band with wide width and hybridize strongly with the $3d$ states through neighboring oxygen $2p$ states. The multiplet structures are taken into account in the $3d^5$ - and $3d^6$ -configurations. Applying the resolvent formalism²⁵ to this model, we calculate the local electronic structure around the tetrahedron sites and thereby the atomic amplitudes of RXS.

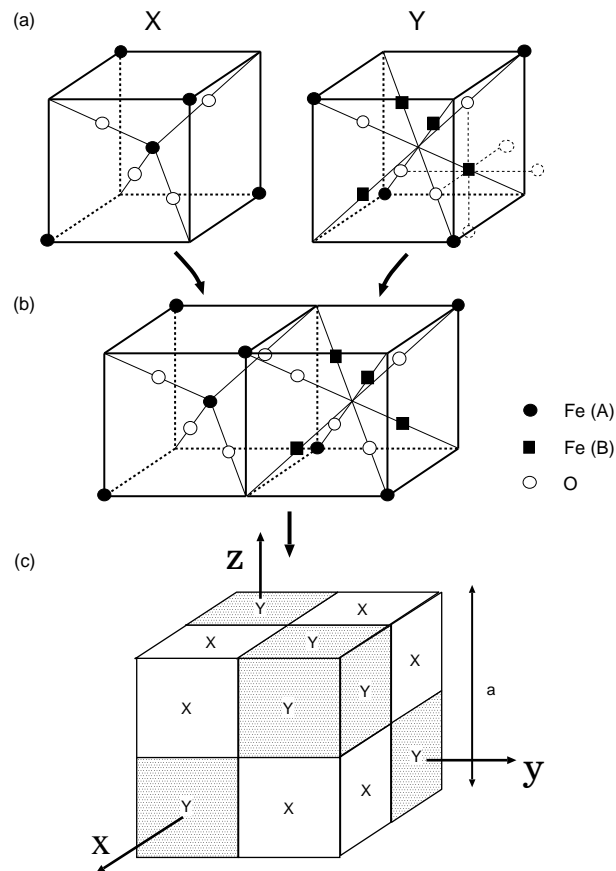


Fig. 1. Crystal structure of magnetite. The origin of coordinates passes through the center of an Fe atom. The unit cell contains 24 Fe atoms.

It is important to recognize that there are two kinds of tetrahedron sites denoted as A_1 and A_2 , that is, one is transformed into the other by space inversion with respect to the center

of the tetrahedron (see Fig. 2). We find that the effective hybridization between the $4p$ and $3d$ states via oxygen $2p$ states changes its sign between the A_1 and A_2 sites, leading to a sign change in the atomic amplitude of the $E1-E2$ process. This is a key point to explain how the pre-edge signals come out. At spots (002) and (006), the contributions from the $E1-E1$ and $E2-E2$ processes as well as Thomson scattering are canceled out in the $\sigma-\sigma'$ channel, and that of the $E1-E2$ process at the A sites only survives in the total scattering amplitude.²⁶ We obtain the pre-edge spectra as a single peak as a function of the photon energy, in agreement with the experiment.^{21,22} Furthermore, we calculate explicitly the dependence on the direction of local magnetic moment in the atomic amplitude. The depending parts are found about an order of magnitude smaller than non-dependent ones. From this calculation, we obtain the intensity differences at spots (002) and (006) when the direction of the magnetization is changed from the $[1, -1, 0]$ direction to the reverse, which shape looks like an "absorption" type as a function of photon energy. It may not be hard to detect these signals, since the magnitudes are about 1/5 to the corresponding pre-edge intensity peaks.

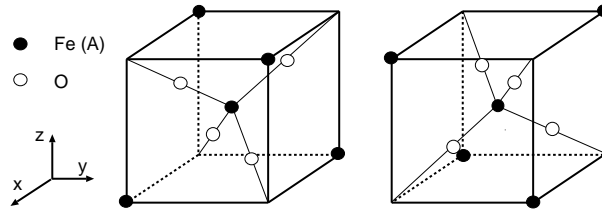


Fig. 2. Two types of tetrahedrons, A_1 (left) and A_2 (right).

We also analyze the dependence on the external magnetic field at spots (222), (333) and (444) in connection with the recent experiment.²⁴ These are allowed spots, where the Thomson scattering amplitude is dominant. Focusing on the $E1-E2$ process at the A sites, we calculate the intensity difference between two opposite directions of the applied magnetic field. The difference arises from the interference between the Thomson scattering amplitude and the $E1-E2$ amplitude. We show that the intensity differences are nearly the same magnitude at both (222) and (333) spots but no difference at (444), and that the shapes as a function of photon energy look like a "dispersion" form concentrated in the pre-edge region. In the experiment by Matsubara *et al.*,²⁴ however, the intensity difference at the (222) spot is distributed over the region much wider than the pre-edge region and two orders of magnitude larger than that at (333) and the calculated values. Also, the spectral shape is quite different from the "dispersion" form. Matsubara *et al.* claimed that the difference at (222) arises from a "magnetolectric" amplitude, that is, a consequence of breaking both centrosymmetry and time-reversal symmetry. We argue that this claim has no ground. Our finding of a "dispersion" form for the intensity difference has been observed in the experiment at the Mn pre- K -edge

in MnCr_2O_4 ,²⁷ where Mn atoms are occupying at the A sites in spinel structure. Since the pre- K -edge signal selects the contribution from the A sites, this experiment suggests that the calculated spectra correspond to the signal from the $E1$ - $E2$ process.

This paper is organized as follows. In Sec. II, we briefly summarize fundamentals of magnetite. In Sec. III, we introduce the model Hamiltonian and study the electronic structure around the A sites. In Sec. IV, we describe the excited states involving a $1s$ -core hole by employing the resolvent formalism. In Sec. V, we calculate the absorption spectra and discuss the x-ray magnetic circular dichroic (XMCD) spectra. We calculate the RXS spectra in comparison with experiments. The last section is devoted to concluding remarks. The geometrical factors are summarized in Appendix.

2. Fundamentals of magnetite

The crystal structure of magnetite is the inverse spinel with the lattice constant $a_0 = 8.396 \text{ \AA}$, as shown in Fig. 1. The unit cell contains 24 iron atoms; 8 iron atoms are tetrahedrally coordinated by 4 oxygens (A sites) and 16 iron atoms are octahedrally coordinated by 6 oxygens (B sites). Note that two types of tetrahedrons exist within the A sites (A_1 and A_2), as shown in Fig. 2. It will be clarified in subsequent sections that the subtle difference in electronic structures between the A_1 and A_2 sites leads to important consequences on the RXS spectra. With disregarding small crystal distortion, we have the position vectors of Fe atoms in the unit cell,

$$\begin{aligned}
 \mathbf{r}_{A_1} & : (0, 0, 0), \left(0, \frac{1}{2}, \frac{1}{2}\right), \left(\frac{1}{2}, 0, \frac{1}{2}\right), \left(\frac{1}{2}, \frac{1}{2}, 0\right), \\
 \mathbf{r}_{A_2} & : \left(\frac{1}{4}, \frac{1}{4}, \frac{1}{4}\right), \left(\frac{1}{4}, \frac{3}{4}, \frac{3}{4}\right), \left(\frac{3}{4}, \frac{1}{4}, \frac{3}{4}\right), \left(\frac{3}{4}, \frac{3}{4}, \frac{1}{4}\right), \\
 \mathbf{r}_B & : \left(\frac{5}{8}, \frac{5}{8}, \frac{5}{8}\right), \left(\frac{5}{8}, \frac{1}{8}, \frac{1}{8}\right), \left(\frac{1}{8}, \frac{5}{8}, \frac{1}{8}\right), \left(\frac{1}{8}, \frac{1}{8}, \frac{5}{8}\right), \\
 & \left(\frac{5}{8}, \frac{7}{8}, \frac{7}{8}\right), \left(\frac{5}{8}, \frac{3}{8}, \frac{3}{8}\right), \left(\frac{1}{8}, \frac{7}{8}, \frac{3}{8}\right), \left(\frac{1}{8}, \frac{3}{8}, \frac{7}{8}\right), \\
 & \left(\frac{7}{8}, \frac{5}{8}, \frac{7}{8}\right), \left(\frac{7}{8}, \frac{1}{8}, \frac{3}{8}\right), \left(\frac{3}{8}, \frac{5}{8}, \frac{3}{8}\right), \left(\frac{3}{8}, \frac{1}{8}, \frac{7}{8}\right), \\
 & \left(\frac{7}{8}, \frac{7}{8}, \frac{5}{8}\right), \left(\frac{7}{8}, \frac{3}{8}, \frac{1}{8}\right), \left(\frac{3}{8}, \frac{7}{8}, \frac{1}{8}\right), \left(\frac{3}{8}, \frac{3}{8}, \frac{5}{8}\right).
 \end{aligned} \tag{2.1}$$

Iron atoms at the A sites are nominally Fe^{3+} , while those at the B sites are a 1 : 1 mixture of Fe^{3+} and Fe^{2+} . Note that Fe^{3+} atoms are in the $3d^5$ -configuration with the spin angular momentum $S = 5/2$, and that Fe^{2+} atoms are in the $3d^6$ -configuration with $S = 2$, according to the Hund rule. The hybridization between the $3d$ states and oxygen $2p$ states may change but slightly the situation. The local magnetic moments are ferromagnetically aligned

within the individual A and B sites, while those at the A and B sites are antiferromagnetically aligned. As a result, a net magnetization remains finite, that is, the magnetite is a ferrimagnet at low temperatures. The Curie temperature is as high as around 850 K. In addition, a metal-insulator transition so called Verwey²⁸ transition takes place around $T = 120$ K. This may be related to charge and orbital orders, which study is outside our scope.^{29–31}

3. Electronic Structures around the A sites

In this section we focus on the electronic structure around the A sites which have no centrosymmetry. In particular, we are interested in the excited states having one $1s$ core hole and one $4p$ electron in accordance with the $E1$ process and those having one $1s$ core hole and one more electron in the $3d$ states in accordance with the $E2$ process.

3.1 Crystal electric field

We start by examining the crystal electric field (CEF) to look for noncentrosymmetric effects. Let charge q be placed at the apexes of a tetrahedron. The electrostatic potential $\phi(x, y, z)$ is expanded around the center as

$$\phi(x, y, z) = \frac{4q}{r_0} \mp \frac{20}{\sqrt{3}} \frac{q}{r_0^4} xyz - \frac{35}{9} \frac{q}{r_0^5} \left(x^4 + y^4 + z^4 - \frac{3}{5} r^4 \right),$$

where $r = \sqrt{x^2 + y^2 + z^2}$ with r_0 being the distance between the origin and the apexes. The last term is well known to represent a split of the energy level of $3d$ states. The second term, which is usually neglected, gives rise to a hybridization between $3d$ and $4p$ states. This coupling comes out because of noncentrosymmetry, but it is much smaller than the same type of coupling arising from the hybridization between the $3d$ and oxygen $2p$ states and between the $4p$ and $2p$ states. The sign $-(+)$ of the coupling is taken for the $A_1(A_2)$ sites.

3.2 Effective hybridization between the $4p$ and $3d$ states

Now we discuss how the $4p$ states could hybridize with the $3d$ states in the absence of centrosymmetry. Let $3d$ wavefunctions be $\psi_{x^2-y^2}^{3d}$, $\psi_{3z^2-r^2}^{3d}$, ψ_{yz}^{3d} , ψ_{zx}^{3d} , and ψ_{xy}^{3d} , and $4p$ wavefunctions be ψ_x^{4p} , ψ_y^{4p} , and ψ_z^{4p} . They are all real and normalized, and have symmetries described in the subscript. Each state could hybridize with a state constructed from a linear combination of oxygen $2p$ wavefunctions at apexes. These oxygen wavefunctions have the same symmetry as their partner of hybridization, which are denoted as $\psi_{x^2-y^2}^{2p}$, $\psi_{3z^2-r^2}^{2p}$, ψ_{yz}^{2p} , ψ_{zx}^{2p} , ψ_{xy}^{2p} , ψ_x^{2p} , ψ_y^{2p} , and ψ_z^{2p} . Using the Slater-Koster two-center integrals given in Table I, we evaluate the strength of hybridization between the $3d$ and $2p$ states and between the $4p$ and $2p$ states,

$$\begin{aligned} t_E^{3d-2p} &= \langle \psi_{x^2-y^2}^{3d} | H_{\text{hyb}}^{3d-2p} | \psi_{x^2-y^2}^{2p} \rangle \\ &= \langle \psi_{3z^2-r^2}^{3d} | H_{\text{hyb}}^{3d-2p} | \psi_{3z^2-r^2}^{2p} \rangle = 1.34 \text{ eV} \end{aligned} \quad (3.1)$$

$$\begin{aligned} t_{T_2}^{3d-2p} &= \langle \psi_{yz}^{3d} | H_{\text{hyb}}^{3d-2p} | \psi_{yz}^{2p} \rangle = \langle \psi_{zx}^{3d} | H_{\text{hyb}}^{3d-2p} | \psi_{zx}^{2p} \rangle \\ &= \langle \psi_{xy}^{3d} | H_{\text{hyb}}^{3d-2p} | \psi_{xy}^{2p} \rangle = \mp 2.33 \text{ eV}, \quad \text{for } A_1(A_2), \end{aligned} \quad (3.2)$$

$$\begin{aligned}
t^{4p-2p} &= \langle \psi_x^{4p} | H_{\text{hyb}}^{4p-2p} | \psi_x^{2p} \rangle = \langle \psi_y^{4p} | H_{\text{hyb}}^{4p-2p} | \psi_y^{2p} \rangle \\
&= \langle \psi_z^{4p} | H_{\text{hyb}}^{4p-2p} | \psi_z^{2p} \rangle = -4.36 \text{ eV},
\end{aligned} \tag{3.3}$$

where H_{hyb}^{3d-2p} and H_{hyb}^{4p-2p} are the hybridization energies between the $3d$ and $2p$ states and between $4p$ and $2p$ states, respectively. The sign $-(+)$ in eq. (3.2) corresponds to the A_1 (A_2) sites. Note that ψ_{yz}^{2p} and ψ_x^{2p} are not identical but have a finite overlap. The same is true for ψ_{zx}^{2p} and ψ_y^{2p} and for ψ_{xy}^{2p} and ψ_z^{2p} , respectively. The overlap is evaluated as

$$S = \langle \psi_x^{2p} | \psi_{yz}^{2p} \rangle = \langle \psi_y^{2p} | \psi_{zx}^{2p} \rangle = \langle \psi_z^{2p} | \psi_{xy}^{2p} \rangle = -0.748. \tag{3.4}$$

Needless to say, these values depend on the phase of wavefunctions constructed from oxygen $2p$ orbitals, but the effective hybridization between the $4p$ and $3d$ states are independent of the phase, since it is proportional to $\langle \psi_x^{4p} | H_{\text{hyb}}^{4p-2p} | \psi_x^{2p} \rangle \langle \psi_x^{2p} | \psi_{yz}^{2p} \rangle \langle \psi_{yz}^{2p} | H_{\text{hyb}}^{3d-2p} | \psi_{yz}^{3d} \rangle$. Its sign is opposite between the A_1 and A_2 sites. This corresponds to the sign change of the second term of eq. (3.1) in the CEF.

3.3 Hamiltonian for a FeO_4 cluster

Now that the $4p$ states could hybridize with the $3d$ states through oxygen $2p$ states, we include oxygen states into our model, in addition to the $1s$, $3d$, and $4p$ states, in order to describe the electronic structure around the A sites. For this reason, we consider the Hamiltonian of a FeO_4 cluster at the A sites,

$$H = H^{3d} + H^{2p} + H_{\text{hyb}}^{3d-2p} + H^{1s} + H^{4p} + H_{\text{hyb}}^{4p-2p}, \tag{3.5}$$

where

$$\begin{aligned}
H^{3d} &= \sum_{m\sigma} E_m^d d_{m\sigma}^\dagger d_{m\sigma} + \frac{1}{2} \sum_{\nu_1 \nu_2 \nu_3 \nu_4} g(\nu_1 \nu_2; \nu_3 \nu_4) d_{\nu_1}^\dagger d_{\nu_2}^\dagger d_{\nu_4} d_{\nu_3} \\
&+ \zeta_{3d} \sum_{mm'\sigma\sigma'} \langle m\sigma | \mathbf{l} \cdot \mathbf{s} | m'\sigma' \rangle d_{m\sigma}^\dagger d_{m'\sigma'} + (\mathbf{H}_{\text{xe}} + \mathbf{H}_{\text{ext}}) \cdot \sum_{m\sigma\sigma'} (\mathbf{s})_{\sigma\sigma'} d_{m\sigma}^\dagger d_{m\sigma'}, \tag{3.6}
\end{aligned}$$

$$H^{2p} = \sum_{m\sigma} E^p p_{m\sigma}^\dagger p_{m\sigma}, \tag{3.7}$$

$$H_{\text{hyb}}^{3d-2p} = \sum_{m\sigma} t_m^{3d-2p} d_{m\sigma}^\dagger p_{m\sigma} + \text{H.c.}, \tag{3.8}$$

$$H^{1s} = \epsilon_{1s} \sum_{\sigma} s_{\sigma}^\dagger s_{\sigma}, \tag{3.9}$$

$$H^{4p} = \sum_{\mathbf{k}\eta\sigma} \epsilon_{4p}(\mathbf{k}) p_{\mathbf{k}\eta\sigma}^\dagger p'_{\mathbf{k}\eta\sigma}, \tag{3.10}$$

$$H_{\text{hyb}}^{4p-2p} = t^{4p-2p} \sum_{\eta\sigma} p_{\eta\sigma}^\dagger p_{\eta\sigma} + \text{H.c.}, \tag{3.11}$$

The H^{3d} describes the energy of $3d$ electrons, where $d_{m\sigma}$ represents an annihilation operator of a $3d$ electron with spin σ and symmetry m ($= x^2 - y^2, 3z^2 - r^2, yz, zx, xy$) at the center. The $3d$ energy level E_m^d is split by the CEF energy $10Dq$. The second term in eq. (3.6) represents the intra-atomic Coulomb interaction with the interaction matrix element $g(\nu_1 \nu_2; \nu_3 \nu_4)$

in terms of F^0 , F^2 , and F^4 (ν stands for (m, σ)). The third term in eq. (3.6) represents the SOI for $3d$ electrons with the SOI coupling ζ_{3d} . We evaluate atomic values of F^2 , F^4 , and ζ_{3d} using the wavefunctions within the Hartree-Fock (HF) approximation,³² and multiply 0.8 to these atomic values with taking account of the slight screening effect.³³ On the other hand, we multiply 0.25 to the atomic value for F^0 , since it is known that F^0 is considerably screened by solid-state effects. The last term in eq. (3.6) describes the energy due to the exchange interaction from neighboring Fe atoms and the Zeeman energy with the external field, where $(\mathbf{s})_{\sigma\sigma'}$ represents the matrix element of the spin operator of the $3d$ electrons. The exchange field \mathbf{H}_{xc} here has a dimension of energy, and is an order $k_{\text{B}}T_c$ with $T_c = 850$ K. The external field \mathbf{H}_{ext} is assumed to be much smaller than \mathbf{H}_{xc} but to be larger than the magnetic anisotropy energy. Therefore it has a role to align the magnetization to the field.

The H^{2p} represents the energy of oxygen $2p$ electrons, where $p_{m\sigma}$ is the annihilation operator of the state $|\psi_m^{2p}\rangle$ with spin σ . The Coulomb interaction is neglected in oxygen $2p$ states. The H_{hyb}^{3d-2p} represent the mixing energy between the $3d$ and $2p$ states, where t_m^{3d-2p} is the matrix element given by eqs. (3.1) and (3.2). The energy of the $2p$ level relative to the $3d$ levels is determined from the charge-transfer energy Δ defined by $\Delta = E^d - E^p + 15U(3d^6) - 10U(3d^5)$ with E^d being an average of E_m^d . Here $U(3d^6)$ and $U(3d^5)$ are the multiplet-averaged d - d Coulomb interaction in the $3d^6$ and $3d^5$ configurations, which are defined by $U = F^0 - (2/63)F^2 - (2/63)F^4$ with F^0 , F^2 , and F^4 .

The last three terms are added to the Hamiltonian in accordance with the excitation of the core electron. The H^{1s} represents the energy of the $1s$ electrons, where s_σ is an annihilation operator of the $1s$ state. The H^{4p} represents the energy of the $4p$ states, which form a band with energy $\epsilon_{4p}(\mathbf{k})$. The H_{hyb}^{4p-2p} represents the hybridization between the $4p$ and oxygen $2p$ states, where $p'_{\eta\sigma}$ is the annihilation operator of $4p$ electron with symmetry $\eta = x, y$, and z , and $p'_{\eta\sigma} = (1/\sqrt{N_0}) \sum_{\mathbf{k}} p'_{\mathbf{k}\eta\sigma}$ (N_0 is the number of \mathbf{k}). This expression could be changed into a form that $4p$ states hybridize with oxygen states symmetrized as yz , zx and xy :

$$H_{\text{hyb}}^{4p-2p} = \tilde{t}^{4p-2p} \sum_{\eta\sigma} p'_{\eta\sigma}^\dagger p_{m\sigma} + \text{H.c.}, \quad (3.12)$$

with $m = yz$ corresponding to $\eta = x$ and so on. Here the matrix element t^{4p-2p} is renormalized as $\tilde{t}^{4p-2p} \equiv t^{4p-2p} S$. We do not explicitly consider the Coulomb interactions between the core hole and the $4p$ and $3d$ electrons, but we could take account of the main effects by adjusting the energy separation between $3d$ level and ϵ_{1s} , since the Slater integrals responsible to the exchange interaction is rather small, $G^2(1s, 3d) = 0.058$ eV.

Table I lists the parameter values used in this paper, which are consistent with the values in the previous calculations.³⁴

Table I. Parameter values for a FeO₄ cluster in the 3d⁵ configuration, measured in units of eV.

$F^0(3d, 3d)$	6.39	$(pd\sigma)_{2p,3d}$	-1.9
$F^2(3d, 3d)$	9.64	$(pd\pi)_{2p,3d}$	0.82
$F^4(3d, 3d)$	6.03	$(pp\sigma)_{2p,4p}$	3.5
ζ_{3d}	0.059	$(pp\pi)_{2p,4p}$	-1.0
Δ	3.5	$10Dq$	-0.7

3.4 Lowest energy state at the A sites

Iron atoms at the A sites are nominally the Fe³⁺ (3d⁵) configuration. The hybridization between the 3d states and oxygen 2p states makes it mix with the 3d⁶ \underline{L} configuration, where \underline{L} indicates the presence of a hole in the ligand oxygen orbitals. Preparing 2352 bases in the 3d⁵ + 3d⁶ \underline{L} configuration, we represent the Hamiltonian $H_{3d} + H_{2p} + H_{\text{hyb}}^{3d-2p}$ for \mathbf{H}_{xc} along the z axis. Diagonalizing numerically the Hamiltonian matrix, we obtain the spin moment $S = 2.40$ and the orbital moment $L = 0.0036$ in the lowest energy state. These values deviate slightly from $S = 5/2$ and $L = 0$ in the lowest state of the 3d⁵ configuration. Note that these values are insensitive to the magnitude and direction of \mathbf{H}_{xc} . The weight of the 3d⁵ and 3d⁶ \underline{L} configurations are obtained as 0.795 and 0.205.

4. Excited states relevant to the K edge RXS

4.1 Resolvent formalism

We use the resolvent formalism in order to describe the excited states containing a 1s core hole and a 4p electron. It is defined by

$$G(z) = [z - H_0 - V]^{-1}, \quad (4.1)$$

where

$$H_0 = H^{3d} + H^{2p} + H^{3d-2p} + H^{1s} + H^{4p}, \quad (4.2)$$

$$V = H_{\text{hyb}}^{4p-2p}. \quad (4.3)$$

Now let $|\beta\rangle$ and $|\gamma\rangle$ be eigenstates of H_0 with energies E_β and E_γ in the configuration of 3d⁵ + 3d⁶ \underline{L} and in the 3d⁶ configuration, respectively. These energies are defined from the ground state energy. The excited states containing a pair of a 4p electron and a 1s-core hole, which is created by the $E1$ transition, may be given by $p_{\eta\sigma}^\dagger s_\sigma |\beta\rangle$. Also the excited states caused by the $E2$ transition may be given by $|c\rangle = s_\sigma |\gamma\rangle$. States $|\beta\rangle$'s span the space of 2352 dimensions, and $|\gamma\rangle$'s span the space of 210 dimensions. Noting that the 1s hole and the 4p electron are coupled to 3d - 2p electrons only through V , we have

$$[G(z)]_{\sigma\gamma, \sigma\gamma'} \equiv \langle \gamma | s_\sigma^\dagger (z - H)^{-1} s_\sigma | \gamma' \rangle$$

$$= \left[(z - E_\gamma + \epsilon_{1s})\delta_{\gamma,\gamma'} - \sum_{\eta\beta} V_{\gamma,\eta\beta} G_0(z - E_\beta) V_{\eta\beta,\gamma'} \right]^{-1}, \quad (4.4)$$

where

$$V_{\eta\beta,\gamma} = \langle \beta | p'_{\eta\sigma} H_{\text{hyb}}^{4p-2p} | \gamma \rangle, \quad (4.5)$$

$$G_0(z) = \frac{1}{N_0} \sum_{\mathbf{k}} \frac{1}{z - \epsilon_{4p}(\mathbf{k}) + \epsilon_{1s} + i\Gamma}, \quad (4.6)$$

with Γ being the core-hole life-time broadening width. The right hand side of eq. (4.4) means the inverse of the matrix whose components are written inside the brace. The inversion of the matrix is numerically carried out.

Once we know $[G(z)]_{\sigma\gamma,\sigma\gamma'}$, we immediately obtain other components of the Green function,

$$\begin{aligned} [G(z)]_{\sigma\eta\beta,\sigma\gamma} &\equiv \langle \beta | s_\sigma^\dagger p'_{\eta\sigma} G(z) s_\sigma | \gamma \rangle \\ &= G_0(z - E_\beta) \sum_{\gamma'} V_{\eta\beta,\gamma'} [G(z)]_{\sigma\gamma',\sigma\gamma}, \end{aligned} \quad (4.7)$$

$$\begin{aligned} G(z)_{\sigma\gamma,\sigma\eta\beta} &\equiv \langle \gamma | s_\sigma^\dagger G(z) p'_{\eta\sigma} s_\sigma | \beta \rangle \\ &= \sum_{\gamma'} [G(z)]_{\sigma\gamma,\sigma\gamma'} V_{\gamma',\eta\beta} G_0(z - E_\beta), \end{aligned} \quad (4.8)$$

$$\begin{aligned} G(z)_{\sigma\eta\beta,\sigma\eta'\beta'} &\equiv \langle \beta | s_\sigma^\dagger p'_{\eta\sigma} G(z) p'_{\eta'\sigma} s_\sigma | \beta' \rangle, \\ &= G_0(z) \delta_{\eta,\eta'} \delta_{\beta,\beta'} \\ &+ G_0(z - E_\beta) \sum_{\gamma\gamma'} V_{\eta\beta,\gamma} [G(z)]_{\sigma\gamma,\sigma\gamma'} V_{\gamma',\eta'\beta'} G_0(z - E_{\beta'}). \end{aligned} \quad (4.9)$$

The Green function is diagonal with the σ variable. It should be noted here that the off-diagonal components, $[G(z)]_{\sigma\eta\beta,\sigma\gamma}$ and $[G(z)]_{\sigma\gamma,\sigma\eta\beta}$ given by eqs. (4.7) and (4.8), change their signs between the A_1 and A_2 sites, in accordance with the change of the effective coupling between $4p$ and $3d$ states. In eq. (4.9), the last term could not appear at the centrosymmetric sites, since it arises from the effective coupling between the $4p$ and $3d$ states which are not allowed within the same site. Note that, if a larger size of cluster is considered, the p -symmetric states could couple to such "3d" states through neighboring iron sites.

Among many $|\beta\rangle$'s in the $3d^5 + 3d^6 \underline{L}$ configuration, the lowest energy state $|\beta_0\rangle$ is taken into account in the following calculation. This may be justified when the presence of the pair of $4p$ electron and $1s$ -core hole could not modify the $3d$ states through the Coulomb interaction. This observation simplifies greatly the analysis of the K-edge RXS in the next section.

5. X-ray absorption and scattering near the K-edge of Iron

5.1 Transition matrix elements

We need to consider two processes around the K -edge; one is the $E1$ process that the $1s$ core electron is excited to the $4p$ states, and the other is the $E2$ process that the $1s$ -core electron is excited to the $3d$ states. These processes may be represented by transition operators,

$$T_{\eta\sigma}^{E1}(j) = M_1 p_{\eta\sigma}^\dagger s_\sigma, \quad T_{m\sigma}^{E2}(j) = M_2 d_{m\sigma}^\dagger s_\sigma, \quad (5.1)$$

where η ($= x, y, z$) and m ($= x^2 - y^2, 3z^2 - r^2, yz, zx, xy$) are connected to the polarization of the incident photon. The annihilation and creation operators are defined with respect to the j th iron site. Since the $1s$ state is well localized around the iron site, M_1 and M_2 are evaluated by using atomic wavefunctions. We have

$$\begin{aligned} M_1 &= iq \int \langle \psi_x^{4p} | x | \psi^{1s} \rangle d^3r \\ &= iq \frac{1}{\sqrt{3}} \int_0^\infty r^3 R_{4p}(r) R_{1s}(r) dr = i 4.46 \times 10^{-3}, \end{aligned} \quad (5.2)$$

$$\begin{aligned} M_2 &= -q^2 \int \langle \psi_{zx}^{3d} | (zx/2) | \psi^{1s} \rangle d^3r \\ &= -q^2 \frac{1}{2\sqrt{15}} \int_0^\infty r^4 R_{3d}(r) R_{1s}(r) dr = -4.07 \times 10^{-4}, \end{aligned} \quad (5.3)$$

where $R_{1s}(r)$, $R_{3d}(r)$, and $R_{4p}(r)$ are radial wavefunctions of the $1s$, $3d$, and $4p$ states, respectively, which are calculated within the HF approximation.³² We have inserted $q \sim 3.6 \times 10^8 \text{ cm}^{-1}$ for the x-ray wavenumber, which corresponds to the K-edge energy 7.12 keV.

5.2 Absorption and XMCD spectra

Although our main concern in this paper is the RXS spectra, we briefly discuss the absorption spectra for looking over the whole K -edge region.

The absorption coefficient may be given by a sum of contributions from each site, since the $1s$ state is well localized at one atomic site. In general, it is decomposed into the contributions of the $E1$ - $E1$, $E1$ - $E2$, $E2$ - $E1$, and $E2$ - $E2$ processes:

$$A_{\eta\eta}^{11}(\omega) = \sum_{j,n,\sigma} \langle g | T_{\eta\sigma}^{E1\dagger}(j) | n \rangle \langle n | T_{\eta\sigma}^{E1}(j) | g \rangle \delta(\omega - E_n + E_g), \quad (5.4)$$

$$A_{\eta m}^{12}(\omega) = \sum_{j,n,\sigma} \langle g | T_{\eta\sigma}^{E1\dagger}(j) | n \rangle \langle n | T_{m\sigma}^{E2}(j) | g \rangle \delta(\omega - E_n + E_g), \quad (5.5)$$

$$A_{m\eta}^{21}(\omega) = \sum_{j,n,\sigma} \langle g | T_{m\sigma}^{E2\dagger}(j) | n \rangle \langle n | T_{\eta\sigma}^{E1}(j) | g \rangle \delta(\omega - E_n + E_g), \quad (5.6)$$

$$A_{mm}^{22}(\omega) = \sum_{j,n,\sigma} \langle g | T_{m\sigma}^{E2\dagger}(j) | n \rangle \langle n | T_{m\sigma}^{E2}(j) | g \rangle \delta(\omega - E_n + E_g), \quad (5.7)$$

where $|g\rangle$ and $|n\rangle$ represent the ground and excited states of the system with energy E_g and E_n . For example, when the x-ray is traveling along the z -direction with the polarization vector

along the x-direction, we need to set $\eta = x$ and $m = zx$. To include the life-time broadening of the core level, we replace the δ -function in eqs. (5.4)-(5.7) by the Lorentzian function with the full width of half maximum $2\Gamma = 1.6$ eV.

In the main K -edge region, the absorption coefficient is given by

$$A_{\eta\eta}^{11}(\omega) = 2|M_1|^2 \left(-\frac{1}{\pi} \right) \text{Im}G_0(\omega), \quad (5.8)$$

where $G_0(\omega)$ is defined by eq. (4.6). It is expressed by the sum over \mathbf{k} and can be replaced by the integral of the $4p$ DOS. It is known in many transition-metal compounds that the absorption spectra are well reproduced in the wide range $20 \sim 30$ eV by means of the $4p$ DOS given by the band calculation.³⁵ In this paper, instead of carrying out the band calculation, we assume the $4p$ DOS rising from the energy corresponding to $\omega = 7111$ eV with the band width as large as 30 eV and sharp cutoff, so that it reproduces the experimental absorption spectra in the main K -edge region (see Fig. 3).

Focusing on the contributions from the A sites in the pre-edge region, we have a more accurate form for $A_{\eta\eta}^{11}(\omega)$. Equation (5.8) is modified by including the last term of eq. (4.9),

$$A_{\eta\eta'}^{11}(\omega) = |M_1|^2 \sum_{\sigma} D_{\sigma\eta\beta_0, \sigma\eta'\beta_0}^{11}(\omega), \quad (5.9)$$

with

$$D_{\sigma\eta\beta_0, \sigma\eta'\beta_0}^{11}(\omega) = \frac{1}{2\pi i} \{ [G(\omega)]_{\sigma\eta'\beta_0, \sigma\eta\beta_0}^* - [G(\omega)]_{\sigma\eta\beta_0, \sigma\eta'\beta_0} \}. \quad (5.10)$$

Here G^* is a complex conjugate of G . Only the lowest energy state $|\beta_0\rangle$ in the $3d^5 + 3d^6 \underline{L}$ configuration, which is equivalent to $|g\rangle$, is considered by the reason explained in the previous section. The contribution of the last term of eq. (4.9) is, however, one order of magnitude smaller than that from the first term, and $A_{\eta\eta}^{11}(\omega)$ is practically determined by eq. (5.8). Note that $A_{\eta\eta}^{11}(\omega)$ could include the contribution of the $3d$ states at further neighbor iron sites if a larger cluster is considered.

The contributions of the $E1$ - $E2$ process, $A_{\eta m}^{12}(\omega)$ and $A_{m\eta}^{21}(\omega)$, are canceled out after summing over the A sites, since they are proportional to $[G(\omega)]_{\sigma\eta\beta_0, \sigma\gamma}$ and $[G(\omega)]_{\sigma\gamma, \sigma\eta\beta_0}$ at each site, and their signs change between at the A_1 and A_2 sites. Therefore, the breaking of centrosymmetry could not influence the absorption spectra.²⁶ The contribution of the $E2$ - $E2$ process is given by

$$A_{mm'}^{22}(\omega) = |M_2|^2 \sum_{\sigma\gamma\gamma'} \langle g | d_{m\sigma} | \gamma \rangle D_{\sigma\gamma, \sigma\gamma'}^{22}(\omega) \langle \gamma' | d_{m'\sigma}^\dagger | g \rangle, \quad (5.11)$$

with

$$D_{\sigma\gamma, \sigma\gamma'}^{22}(\omega) = \frac{1}{2\pi i} \{ [G(\omega)]_{\sigma\gamma', \sigma\gamma}^* - [G(\omega)]_{\sigma\gamma, \sigma\gamma'} \}. \quad (5.12)$$

The upper panel in Fig. 3 shows the calculated absorption spectra in comparison with the experiment.³⁶ Any reliable theoretical estimates of the core-level energy are not available.

In addition, the K -edge energy is different for different experiments.^{22–24} Therefore, we have tentatively adjusted the energy separation between the $1s$ -core level and the $4p$ states. Since $A_{mm}^{22}(\omega)$ is limited within the pre-edge region, the spectra in the main K -edge region are dominated by $A_{\eta\eta}^{11}(\omega)$. The band bottom of the $4p$ DOS corresponds to $\omega = 7111$ eV. A tail in $A_{\eta\eta}^{11}(\omega)$ due to Γ gives a substantial contribution in the pre-edge region, as shown in the inset in the figure. The total intensity in the pre-edge region is underestimated in comparison with the experiment.³⁶

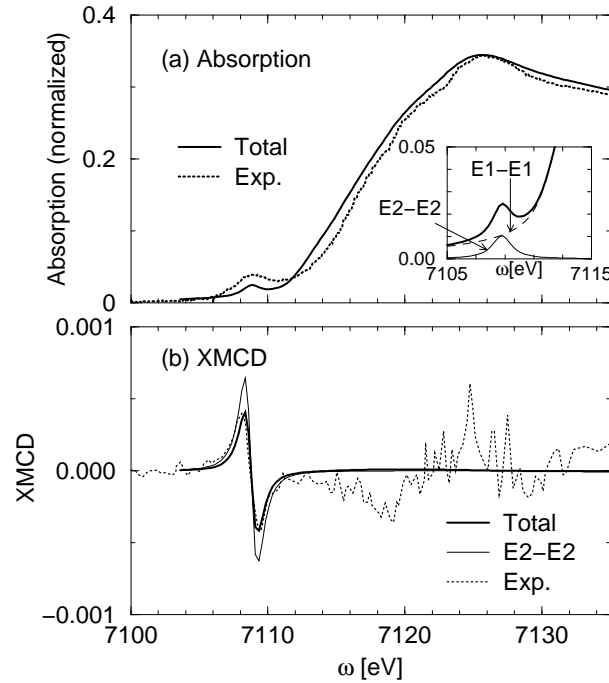


Fig. 3. Absorption coefficient (upper) and XMCD spectra (lower) as a function of photon energy. The solid and dotted lines represent the calculated and the experimental spectra,³⁶ respectively. The inset is the decomposition of the total spectrum into $A^{11}(\omega)$ and $A^{22}(\omega)$ in the pre-edge region.

When the x-ray is traveling along the direction opposite to the magnetization, the absorption coefficient is different between the right-hand and left-hand circular polarizations. The XMCD is defined by the difference between them. It is known that the XMCD is brought about by the SOI. We neglect the SOI on the $4p$ states, since its effect is expected to be very small in the pre-edge region. The lower panel in Fig. 3 shows the calculated XMCD spectra in comparison with the experiment.³⁶ The calculated difference is divided by the value at the peak of the main edge in the absorption coefficient. Since no scale is shown for the XMCD spectra in ref. 36, the experimental curve is drawn in arbitrary scale. The $E2-E2$ process gives the largest contribution.

Note that these results are obtained for the A sites. For the B sites, the main K -edge

spectra are the same, but the pre-edge spectra could be different. We need to consider the contribution from the B sites for quantitative comparison with the experiment.

5.3 RXS spectra

We consider the scattering geometry as illustrated in Fig. 4, where the incident x-ray with momentum \mathbf{k} , energy ω , polarization ϵ is scattered into the state with momentum \mathbf{k}' , energy ω , polarization ϵ' . We define the scattering vector by $\mathbf{G} \equiv \mathbf{k}' - \mathbf{k}$.³⁷

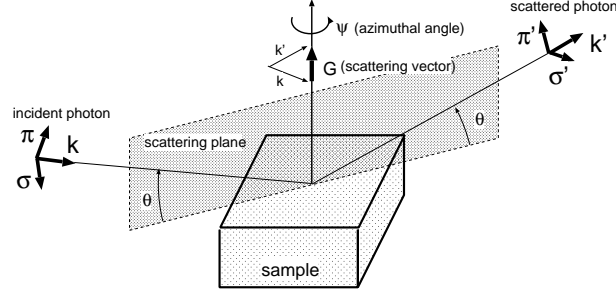


Fig. 4. Scattering geometry. Incident x-ray with momentum \mathbf{k} and polarization σ or π is scattered into the state with momentum \mathbf{k}' and polarization σ' or π' .

By the same reason as the case of the absorption spectra, the RXS amplitude may be given by a sum of amplitudes from each iron site. Then the scattering amplitude per unit cell is expressed as

$$\begin{aligned}
 F(\mathbf{G}, \omega) &= r_0 \left[F^{\text{Th}}(\mathbf{G}) \epsilon \cdot \epsilon' + \sum_{\eta, \eta'} P_{\eta'}^{\mu'} F_{\eta' \eta}^{11}(\mathbf{G}, \omega) P_{\eta}^{\mu} + \sum_{\eta, m} P_{\eta'}^{\mu'} F_{\eta' m}^{12}(\mathbf{G}, \omega) Q_m^{\mu} \right. \\
 &\quad \left. + \sum_{m', \eta} Q_{m'}^{\mu'} F_{m' \eta}^{21}(\mathbf{G}, \omega) P_{\eta}^{\mu} + \sum_{m', m} Q_{m'}^{\mu'} F_{m' m}^{22}(\mathbf{G}, \omega) Q_m^{\mu} \right], \quad (5.13)
 \end{aligned}$$

where the classical electron radius $r_0 \equiv e^2/(mc^2) = 2.82 \times 10^{-13}$ cm. The first term represents Thomson scattering, which may be estimated as

$$F^{\text{Th}}(\mathbf{G}) = \sum_j f_j^0(\mathbf{G}) \exp(-i\mathbf{G} \cdot \mathbf{r}_j), \quad (5.14)$$

where $f_j^0(\mathbf{G})$ is the atomic form factor with j running over not only iron sites but also oxygen sites.

The remaining terms represent resonant scattering. They are defined by

$$F_{\zeta', \zeta}^{\lambda', \lambda}(\mathbf{G}, \omega) = \sum_j f_j^{\lambda', \lambda}(\omega)_{\zeta', \zeta} \exp(-i\mathbf{G} \cdot \mathbf{r}_j), \quad \lambda, \lambda' = 1, 2, \quad (5.15)$$

where $f_j^{\lambda', \lambda}(\omega)_{\zeta', \zeta}$ is the resonant scattering amplitude at the j th iron site in the unit cell. For example, $f_j^{12}(\omega)$ is defined by

$$f_j^{12}(\omega)_{\eta m} = mc^2 \sum_{n\sigma} \frac{\langle g | T_{\eta\sigma}^{\text{E}1\dagger}(j) | n \rangle \langle n | T_{m\sigma}^{\text{E}2}(j) | g \rangle}{\omega - E_n + E_g + i\Gamma}. \quad (5.16)$$

Other components are similarly defined. In eq. (5.13), P_η^μ and Q_m^μ represent the geometrical factors of the E1 and E2 transitions for the incident x-ray with polarization $\mu = \sigma$ or π , while $P_\eta^{\mu'}$ and $Q_m^{\mu'}$ represent those for the scattered x-ray with polarization $\mu' = \sigma'$ or π' . Their general expressions are summarized in Appendix.

The resonant terms at the A sites are expressed by using the resolvent given in Sec. III:

$$f_A^{11}(\omega)_{\eta'\eta} = mc^2 |M_1|^2 \sum_{\sigma} [G(\omega)]_{\sigma\eta',\sigma\eta}, \quad (5.17)$$

$$f_A^{12}(\omega)_{\eta'm} = mc^2 M_1^* M_2 \sum_{\sigma\gamma} [G(\omega)]_{\sigma\eta'\beta_0,\sigma\gamma} \langle \gamma | d_{m\sigma}^\dagger | g \rangle, \quad (5.18)$$

$$f_A^{21}(\omega)_{m'\eta} = mc^2 M_2^* M_1 \sum_{\sigma\gamma} \langle g | d_{m'\sigma} | \gamma \rangle [G(\omega)]_{\sigma\gamma,\sigma\eta\beta_0}, \quad (5.19)$$

$$f_A^{22}(\omega)_{m'm} = mc^2 |M_2|^2 \sum_{\sigma\gamma\gamma'} \langle g | d_{m'\sigma} | \gamma \rangle [G(\omega)]_{\sigma\gamma,\sigma\gamma'} \langle \gamma' | d_{m\sigma} | g \rangle. \quad (5.20)$$

Amplitudes $f_A^{12}(\omega)_{\eta'm}$ and $f_A^{21}(\omega)_{m'\eta}$ change their signs between the A₁ and A₂ sites, respectively. They depend also on the direction of the local magnetic moment. A careful examination of eqs. (5.18) and (5.19) leads us to the expression,

$$f_A^{12}(\omega) = \begin{matrix} x \\ y \\ z \end{matrix} \begin{pmatrix} x^2 - y^2 & 3z^2 - r^2 & yz & zx & xy \\ b(\omega)n_x & c(\omega)n_x & a(\omega) & -d(\omega)n_z & d(\omega)n_y \\ b(\omega)n_y & -c(\omega)n_y & d(\omega)n_z & a(\omega) & -d(\omega)n_x \\ -2b(\omega)n_z & 0 & -d(\omega)n_y & d(\omega)n_x & a(\omega) \end{pmatrix}, \quad (5.21)$$

$$f_A^{21}(\omega) = \begin{matrix} x^2 - y^2 \\ 3z^2 - r^2 \\ yz \\ zx \\ xy \end{matrix} \begin{pmatrix} x & y & z \\ b(\omega)n_x & b(\omega)n_y & -2b(\omega)n_z \\ c(\omega)n_x & -c(\omega)n_y & 0 \\ -a(\omega) & d(\omega)n_z & -d(\omega)n_y \\ -d(\omega)n_z & -a(\omega) & d(\omega)n_x \\ d(\omega)n_y & -d(\omega)n_x & -a(\omega) \end{pmatrix}, \quad (5.22)$$

where (n_x, n_y, n_z) represents the direction cosine of the local magnetic moment vector centered at each iron atom. Note that the local magnetic moment at the A sites is opposite to the total magnetization. The component $a(\omega)$, which is independent of the direction of the local magnetic moment, exists even in the absence of the SOI. On the other hand, $b(\omega)$, $c(\omega)$, and $d(\omega)$, which are one order of magnitude smaller than $a(\omega)$, disappear without the SOI. All these components are appreciable only in a narrow pre-edge region.

For the resonant terms at the B sites, $f_B^{11}(\omega)$ may be expressed by

$$f_B^{11}(\omega)_{\eta'\eta} = mc^2 |M_1|^2 2G_0(\omega) \delta_{\eta'\eta}, \quad (5.23)$$

where the contribution like the last term of eq. (4.9) does not exist. The $f_B^{12}(\omega)$ and $f_B^{21}(\omega)$ disappear because of centrosymmetry. We expect $|f_B^{22}(\omega)| \ll |f_B^{11}(\omega)|$ in the pre-edge region.

This contrast with the absorption coefficient, where the $E2$ - $E2$ contribution is comparable to the $E1$ - $E1$ contribution. The reason is that the scattering amplitude is affected by $G_0(\omega)$ itself, whose real part is about two orders of magnitude larger than the imaginary part, while only the imaginary part contributes to the absorption coefficient. Note that, though it is small, $f_B^{22}(\omega)$ could give rise to the magnetic scattering amplitude, which study is outside of the purpose of this paper.

In the following, we analyze the RXS spectra at several Bragg spots, focusing on the $\sigma - \sigma'$ channel.

5.3.1 $\mathbf{G} = (002)$ and (006)

For position vectors given by eq. (2.1), the phase factors $\exp(-i\mathbf{G} \cdot \mathbf{r}_j)$ are 1 at the A_1 sites, -1 at the A_2 sites, and $\mp i, \mp i, \mp i, \mp i, \pm i, \mp i, \mp i, \mp i, \mp i$ (upper and lower signs correspond to (002) and (006) , respectively) at the B sites. Thomson scattering amplitude as well as all the resonant terms are canceled out except for $f_A^{12}(\omega)$ and $f_A^{21}(\omega)$, due to the phase factors. Therefore, these Bragg spots are suitable to investigate non-centrosymmetric effects on the RXS. Several experiments of RXS have actually been carried out on these spots,^{21,22} but the dependence of the spectra on the magnetization direction has not been studied yet. We calculate the RXS spectra and analyze such dependence.

We consider the situation that the scattering plane contains a vector $(1, -1, 0)$ (see Fig. 4). The geometrical factors $P^\sigma, P^{\sigma'}, Q^\sigma$, and $Q^{\sigma'}$ are given by putting $\psi = \pi/4$ in the expressions in Appendix. We assume that the local magnetic moment on the A sites is along the $\mathbf{n} = (n_x, n_y, 0)$ direction. Then, using eqs. (5.21) and (5.22), we have the scattering amplitude in the $\sigma - \sigma'$ channel,

$$\begin{aligned} F(\mathbf{G}, \omega) &= r_0 \sum_{\eta, m} \left[P_\eta^{\sigma'} F_{\eta m}^{12}(\mathbf{G}, \omega) Q_m^\sigma + Q_m^{\sigma'} F_{m \eta}^{21}(\mathbf{G}, \omega) P_\eta^\sigma \right] \\ &= 8r_0 [2 \sin \theta a(\omega) + \sqrt{2}(n_x - n_y) \cos \theta b(\omega)], \end{aligned} \quad (5.24)$$

where Bragg angle θ is 12.0 and 38.5 degrees for (002) and (006) , respectively. Let $I_+(\mathbf{G}, \omega)$ and $I_-(\mathbf{G}, \omega)$ be the intensities per unit cell for the direction of the magnetic moment \mathbf{n} and the reverse, respectively. Then the average and the difference of the intensities are given by

$$\begin{aligned} I^{\sigma-\sigma'}(\mathbf{G}, \omega) &\equiv \frac{1}{2} \left(I_+^{\sigma-\sigma'}(\mathbf{G}, \omega) + I_-^{\sigma-\sigma'}(\mathbf{G}, \omega) \right) \\ &= 256r_0^2 \left\{ \sin^2 \theta |a(\omega)|^2 + \frac{1}{2} \cos^2 \theta (n_x - n_y)^2 |b(\omega)|^2 \right\}, \end{aligned} \quad (5.25)$$

$$\begin{aligned} \Delta I^{\sigma-\sigma'}(\mathbf{G}, \omega) &\equiv I_+^{\sigma-\sigma'}(\mathbf{G}, \omega) - I_-^{\sigma-\sigma'}(\mathbf{G}, \omega) \\ &= 128\sqrt{2}r_0^2 \sin 2\theta (n_x - n_y) [a(\omega)^* b(\omega) + \text{c.c.}]. \end{aligned} \quad (5.26)$$

Since $b(\omega)$ is one order of magnitude smaller than $a(\omega)$, the average intensity $I^{\sigma-\sigma'}(\omega)$ is dominated by $|a(\omega)|^2$. On the other hand, the difference spectra arise from the interference between the terms of $a(\omega)$ and $b(\omega)$.

Figure 5 shows $I^{\sigma-\sigma'}(\mathbf{G}, \omega)$ and $\Delta I^{\sigma-\sigma'}(\mathbf{G}, \omega)$ calculated with $\mathbf{n} = (1/\sqrt{2}, -1/\sqrt{2}, 0)$. This magnetization direction corresponds to the magnetic field applied along the $[-1, 1, 0]$ direction. The $I^{\sigma-\sigma'}(\mathbf{G}, \omega)$ is concentrated in a narrow pre-edge region, and becomes larger for $\mathbf{G} = (006)$, in consistent with the experiments.^{21,22} The $\Delta I^{\sigma-\sigma'}(\mathbf{G}, \omega)$ is relatively large, only one order of magnitude smaller than the average intensity. This intensity difference is a consequence of breaking both the local centrosymmetry and the time-reversal symmetry. It would not be hard to detect such a difference.

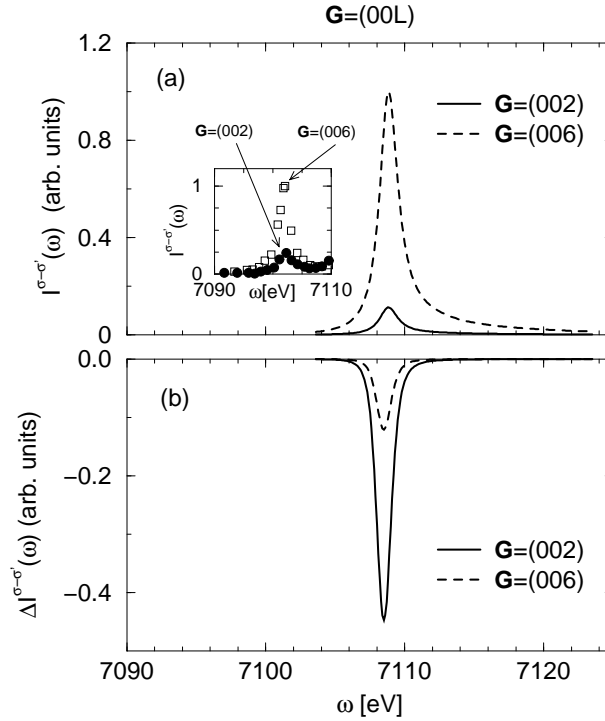


Fig. 5. Scattering intensity as a function of photon energy in the pre-edge region in the $\sigma-\sigma'$ channel. Panel (a) shows the average intensity. Panel (b) shows the intensity difference when the magnetic field is applied along the $[-1, 1, 0]$ direction and the reverse, which is divided by the peak value of the average intensity. The solid and broken lines represent the intensities for $\mathbf{G} = (002)$ and (006) , respectively. The inset on panel (a) represents the experimental curves taken from ref. 22.

5.3.2 $\mathbf{G} = (222)$

For position vectors given by eq. (2.1), the phase factors $\exp(-i\mathbf{G} \cdot \mathbf{r}_j)$ are 1 at the A_1 sites, -1 at the A_2 sites, and i at all B sites. Therefore this spot is not prohibited.

Thomson scattering gives the largest contribution; the contribution from the A sites are canceled out, but those from the B sites and oxygen sites remain, resulting in

$$F^{\text{Th}}(\mathbf{G}) = 16if_B - 32if_O, \quad (5.27)$$

Table II. $F^{\text{Th}}(\mathbf{G})$ and $F^{11}(\mathbf{G}, \omega_0)$ with ω_0 being the pre-edge absorption peak.

hkl	$F^{\text{Th}}(\mathbf{G})$	$[F^{11}(\mathbf{G}, \omega_0)]_{\eta\eta}$
(222)	$i 123.1$	$0.68 - i 10.24$
(333)	$148.7 - i 148.7$	$-32.52 + i 5.78$

where $f_B = (1/2)[f(\text{Fe}^{2+}) + f(\text{Fe}^{3+})]$ is the form factor of iron at the B sites and $f_O = f(\text{O}^{2-})$ is that of oxygen. They are evaluated from the atomic values tabulated in ref. 38. As regards the resonant terms, $f_A^{11}(\omega)$ and $f_A^{22}(\omega)$ are canceled out at the A sites due to the phase factor, but the contribution from the B sites remains. We have

$$[F^{11}(\mathbf{G}, \omega)]_{\eta'\eta} \equiv F_0^{11}(\mathbf{G}, \omega)\delta_{\eta'\eta} = 16if_B^{11}(\omega)\delta_{\eta'\eta}, \quad (5.28)$$

where $f_B^{11}(\omega)$ is evaluated from eq. (5.23). Note that the atomic calculation of $f_B^{11}(\omega)$ would contain large errors in the pre-edge region, because a single level of $4p$ states in an atom changes into an energy band with width as large as ~ 20 eV in solids. We list the calculated values in Table II. The Thomson scattering amplitude is much larger than the resonant term. These values are much larger than those reported in ref. 24. Thus, the average intensity is given by

$$I^{\sigma-\sigma'}(\mathbf{G}, \omega) = r_0^2 |F^{\text{Th}}(\mathbf{G}) + F_0^{11}(\mathbf{G}, \omega)|^2. \quad (5.29)$$

Next we analyze the dependence on the direction of applied magnetic field in accordance with the experiment.²⁴ The scattering plane is set to contain a vector $(1, -1, 0)$ with applying magnetic field along the $[11\bar{2}]$ direction and the reverse. The geometrical factors P^σ , $P^{\sigma'}$, Q^σ , and $Q^{\sigma'}$ are given by putting $\psi = \pi/4$ in the expressions in Appendix. Substituting $(\mp 1/\sqrt{6}, \mp 1/\sqrt{6}, \pm 2/\sqrt{6})$ for (n_x, n_y, n_z) in eqs. (5.21) and (5.22), we obtain the scattering amplitude in the $\sigma - \sigma'$ channel,

$$\sum_{\eta, m} \left[P_\eta^{\sigma'} [F^{12}(\mathbf{G}, \omega)]_{\eta m} Q_m^\sigma + Q_m^{\sigma'} [F^{21}(\mathbf{G}, \omega)]_{m \eta} P_\eta^\sigma \right] = 8 \cos \theta [\delta_0 a(\omega) \pm \delta_1 c(\omega) \pm \delta_2 d(\omega)], \quad (5.30)$$

where the upper (lower) signs correspond to upper (lower) signs of (n_x, n_y, n_z) , and $\delta_0 = -(2/3)(1/\sqrt{2} + 2/\sqrt{3})$, $\delta_1 = -\sqrt{2}/3$, $\delta_2 = (2/3)(1 - \sqrt{2/3})$. Bragg angle θ is 21.1 degrees. Since the direction of the local magnetic moment on the A sites is opposite to the direction of the applied magnetic field, we define the intensity difference as the value with the upper sign for \mathbf{n} minus the value with the lower sign for \mathbf{n} . As a consequence, we have

$$\Delta I^{\sigma-\sigma'}(\omega) = 16r_0^2 \cos \theta \{ [F^{\text{Th}}(\mathbf{G})^* + F_0^{11}(\omega)^*] [\delta_1 c(\omega) + \delta_2 d(\omega)] + \text{c.c.} \}. \quad (5.31)$$

The intensity difference arises from the interference between the term of $F^{\text{Th}}(\mathbf{G}) + F_0^{11}(\mathbf{G}, \omega)$ and the terms of $c(\omega)$ and $d(\omega)$.

Figure 6 shows the relative intensity difference $\Delta I^{\sigma-\sigma'}(\mathbf{G}, \omega)/I^{\sigma-\sigma'}(\mathbf{G}, \omega)$ in the pre-edge region. The spectral shape takes a peculiar "dispersion" form. This may be explained

as follows. The factor $F^{\text{Th}}(\mathbf{G}) + F^{11}(\mathbf{G}, \omega)$ at (222) spot is very close to a pure imaginary number as shown in Table II. Another factor $c(\omega)$ or $d(\omega)$ is given by a resolvent matrix element multiplied by $M_1^* M_2$ which is a pure imaginary number. Thereby the product of the two factors in eq. (5.31) becomes a resolvent matrix element multiplied by a real number. By adding its complex conjugate, eq. (5.31) becomes proportional to the real part of the resolvent matrix element. The real part of the Green function usually takes a "dispersion" form as a function of energy.

The intensity difference in the experiment by Matsubara *et al.*²⁴ is different from the one calculated here. It extends over a region much wider than the region of the pre-edge absorption spectra with an order of magnitude larger intensity, which behavior is quite unusual. Also the shape is different from a "dispersion" form. Matsubara *et al.* claimed that the spectra they found arise from a "magnetoelectric" amplitude, that is, a consequence of breaking both the centrosymmetry and the time-reversal symmetry. According to the present analysis, this claim has no ground. In this connection, we would like to draw attention to the similar RXS experiment for MnCr_2O_4 , where the shape and strength quite similar to the curve calculated above have been observed at the Mn pre-K-edge.²⁷ In this material, Mn atoms occupy at the A sites in spinel structure. Since the Mn pre-edge spectrum selects only the A site contribution, this experimental result indicates that the calculated spectra correspond to the "magnetoelectric" signal. Note that a similar "dispersion" form of the spectra has been observed¹⁶ and theoretically analyzed^{17,18} at the Fe *K* edge of GaFeO_3 .

Finally we comment on what happens on the intensity difference when the scattering vector is reversed. Different from the conventional case, the signal is reversed with keeping the shape, as shown in Fig. 6. The $F^{12}(\mathbf{G}, \omega)$ and $F^{21}(\mathbf{G}, \omega)$ are unaltered because the phase factors at the A sites are the same with reversing \mathbf{G} . On the other hand, $F^{\text{Th}}(\mathbf{G}) + F^{11}(\mathbf{G}, \omega)$ changes its sign, because the phase factors at the B sites is changed from i to $-i$, resulting in the sign change in eq. (5.31).

5.4 $\mathbf{G} = (333)$

The phase factors $\exp(-i\mathbf{G} \cdot \mathbf{r}_j)$ are 1 at the A_1 sites, $-i$ at the A_2 sites, $\exp(i3\pi/4)$, $\exp(i3\pi/4)$, $\exp(i3\pi/4)$, $\exp(i3\pi/4)$, $\exp(-i\pi/4)$, $\exp(i\pi/4)$, $\exp(i\pi/4)$, $\exp(i\pi/4)$, $\exp(i\pi/4)$ at the B sites, respectively. The Thomson scattering amplitude and the resonant term $F^{11}(\mathbf{G}, \omega)$ are given by

$$F^{\text{Th}}(\mathbf{G}) = 4(1 - i)(f_A + \sqrt{2}f_B), \quad (5.32)$$

$$F^{11}(\mathbf{G}, \omega)_{\eta'\eta} \equiv F_0^{11}(\mathbf{G}, \omega)\delta_{\eta'\eta} = 4(1 - i)[f_A^{11}(\omega) + \sqrt{2}f_B^{11}(\omega)]\delta_{\eta'\eta}. \quad (5.33)$$

These amplitudes are evaluated by using atomic form factors for f_A and f_B and eq. (5.23) for $f_A^{11}(\omega)$ and $f_B^{11}(\omega)$. The results which are listed in Table II. In addition, we have the E_1 - E_2

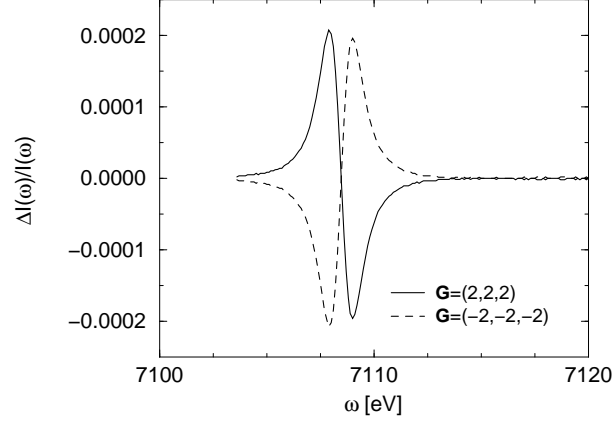


Fig. 6. Relative intensity difference $\Delta I^{\sigma-\sigma'}(\mathbf{G}, \omega)/I^{\sigma-\sigma'}(\mathbf{G}, \omega)$ as a function of photon energy at $\mathbf{G} = (222)$ and $\mathbf{G} = (\overline{222})$ in the pre-edge region.

term,

$$\sum_{\eta, m} \left[P_{\eta}^{\sigma'} [F^{12}(\mathbf{G}, \omega)]_{\eta m} Q_m^{\sigma} + Q_m^{\sigma'} [F^{21}(\mathbf{G}, \omega)]_{m \eta} P_{\eta}^{\sigma} \right] = 4(1+i) \cos \theta [\delta_0 a(\omega) \pm \delta_1 c(\omega) \pm \delta_2 d(\omega)], \quad (5.34)$$

with Bragg angle $\theta = 32.6$ degrees. As a result, we obtain the intensity difference as

$$\Delta I^{\sigma-\sigma'}(\omega) = 8r_0^2 \cos \theta \{ [F^{\text{Th}}(\mathbf{G})^* + F_0^{11}(\omega)^*] (1+i) [\delta_1 c(\omega) + \delta_2 d(\omega)] + \text{c.c.} \}. \quad (5.35)$$

Since $F^{\text{Th}}(\mathbf{G})^*$ is proportional to $(1+i)$, the right hand side of eq. (5.35) is nearly proportional to the real part of a resolvent matrix element. Therefore we would expect a “dispersion” form of spectra as a function of photon energy.

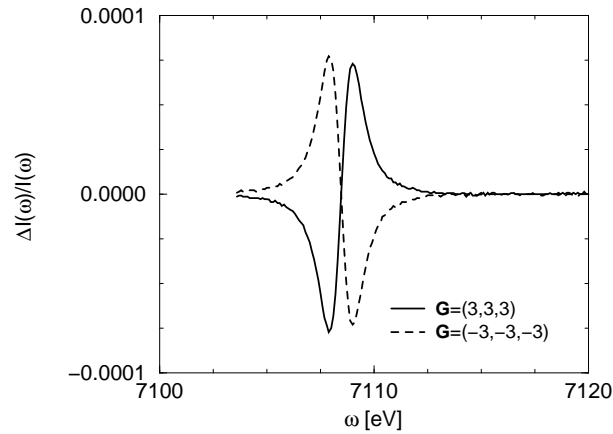


Fig. 7. Relative intensity difference $\Delta I^{\sigma-\sigma'}(\mathbf{G}, \omega)/I^{\sigma-\sigma'}(\mathbf{G}, \omega)$ as a function of photon energy at $\mathbf{G} = (333)$ and $\mathbf{G} = (\overline{333})$ in the pre-edge region.

Figure 7 shows the relative intensity difference $\Delta I^{\sigma-\sigma'}(\mathbf{G}, \omega)/I^{\sigma-\sigma'}(\mathbf{G}, \omega)$ thus evaluated.

The calculated value has the same size of magnitude as the experimental one²⁴ and is nearly half of the calculated one for (222). Note that the experimental value at (222) is about two order of magnitude larger than the values at (333).

5.5 $\mathbf{G} = (444)$

The phase factors $\exp(-i\mathbf{G} \cdot \mathbf{r}_j)$ are 1 at the A sites and -1 at the B sites. Therefore, the $E1-E2$ terms $F^{12}(\mathbf{G}, \omega)$ and $F^{21}(\mathbf{G}, \omega)$ vanish due to the cancellation between the A_1 and A_2 sites. In the experiment,²⁴ the intensity dependence is found negligible. If we take seriously this fact, it means that the contribution of the magnetic scattering amplitude $F^{22}(\mathbf{G}, \omega)$ is quite small.

6. Concluding Remarks

We have studied how the breaking of centrosymmetry affects the RXS spectra through a microscopic calculation for magnetite. The centrosymmetry is locally broken at tetrahedral (A) sites. In such a circumstance, the $4p$ states strongly hybridize with the $3d$ states through neighboring oxygen $2p$ states, giving rise to the non-vanishing contribution of the $E1-E2$ process in the RXS spectra. This observation is substantiated by introducing a microscopic model of a FeO_4 cluster with the $4p$ states forming a band and the $3d$ states forming multiplet structures. We have calculated the RXS spectra with the help of the resolvent formalism. It is shown that the hybridization changes its sign between the A_1 and A_2 sites and accordingly the local amplitude from the $E1-E2$ process changes its sign. This sign change causes non-vanishing RXS intensities at the forbidden spots (002) and (006). The spectra are concentrated in a narrow pre-edge region with intensities larger at (006) than at (002), in agreement with the experiment. In addition, we have carefully analyzed the scattering matrix for the $E1-E2$ process, which depends on the direction of the applied magnetic field. Such dependence is only possible when both centrosymmetry and time-reversal symmetry are broken. Through this analysis, we have obtained large dependences of intensity at (002) and (006) spots. We hope that this dependence could be observed in future experiments.

We have also analyzed the dependence on the direction of the applied magnetic field at (222), (333) and (444) spots in connection with the experiment. These spots are allowed with large Thomson scattering amplitudes. Having calculated the intensities for two opposite directions of the applied magnetic field, we have obtained their difference with the same order of magnitude at both (222) and (333) spots but negligible difference at (444). The intensity difference is found to have a “dispersion” form as a function of photon energy, which is concentrated in a narrow pre-edge region. In the experiment by Matsubara *et al.*,²⁴ however, the intensity difference at the (222) spot is distributed over the region much wider than the pre-edge region with the spectral shape quite different from the “dispersion” form. The observed intensity difference at (222) is two orders of magnitude larger than the one at (333). These behaviors seem unusual and hard to explain. Matsubara *et al.* claimed that the difference at

the (222) spot arises from a “magnetoelectric” amplitude, that is, a consequence of breaking both centrosymmetry and time-reversal symmetry. This claim has no ground, according to the analysis in this paper. A “dispersion” form of spectral shape has been observed in the experiment at the Mn pre- K -edge in MnCr_2O_4 .²⁷ Since Mn atoms are occupying at the A sites in spinel structure, the pre- K -edge signal selects the contribution from the A sites. This experiment suggests that the calculated spectra correspond to the “magnetoelectric” signal in the magnetite. The large signal at the (222) spot might be related to B sites. We hope experiments in future clarify the situation in magnetite.

Acknowledgments

We would like to thank Dr. Matsubara for providing us with his thesis and for valuable discussions. This work was partly supported by Grant-in-Aid for Scientific Research from the Ministry of Education, Culture, Sport, Science, and Technology, Japan.

Appendix: Geometrical factors

We briefly describe a derivation of geometrical factors. A geometrical setting of x-ray scattering adopted in the present work is shown in Fig. 4. We introduce three coordinate systems, (x', y', z') , (x'', y'', z'') , and (x''', y''', z''') . The first coordinate system is attached to the incident (scattered) photon with its z' axis being parallel to $\mathbf{k}(\mathbf{k}')$. Its x' and y' axes are perpendicular and parallel to the scattering plane, respectively. The second coordinate system is used as the definition of the origin of the azimuthal angle ψ . Its z'' axis is aligned to \mathbf{G} direction and y'' axis is in the scattering plane at $\psi = 0$ with $x'' = x'$. The third coordinate system is fixed to the crystal.

These three coordinate systems can be connected by the Euler rotation with the choices of appropriate Euler angles. Here we use the same definition of the Euler rotation adopted in Rose’s book.³⁹ From (x'', y'', z'') to (x', y', z') coordinate systems, the Euler angles are chosen as $(\frac{\pi}{2}, \frac{\pi}{2} \pm \theta, -\frac{\pi}{2})$ where θ represents the Bragg angle. The upper (lower) sign is for the incident (scattered) photon. Hereafter, we restrict our discussion on the incident photon case alone, since the results for the scattered photon are obtained by replacing every θ with $-\theta$. The Euler angles of the rotation from the (x'', y'', z'') coordinate system to the (x''', y''', z''') coordinate system are given by $(\alpha, \beta, 0)$ where α and β are the azimuthal and the polar angles of \mathbf{G} , respectively.

In order to calculate the geometrical factors, we start with writing down the basis corresponding to the σ and π polarizations. For dipole transition, it is simple since $\boldsymbol{\epsilon}^\sigma = \mathbf{e}_{x'}$ and $\boldsymbol{\epsilon}^\pi = -\mathbf{e}_{y'}$ hold in the present setting. Here \mathbf{e}_j denotes the unit vector directed to j axis. Then, the geometrical factors $\{P_j^\mu\}$ ($\mu = \sigma, \pi$) are defined by the following relations.

$$\boldsymbol{\epsilon}^\sigma \cdot \mathbf{r} = x' = P_x^\sigma x''' + P_y^\sigma y''' + P_z^\sigma z''', \quad (\text{A}\cdot 1)$$

$$\boldsymbol{\epsilon}^\pi \cdot \mathbf{r} = -y' = P_x^\pi x''' + P_y^\pi y''' + P_z^\pi z''', \quad (\text{A}\cdot 2)$$

where \mathbf{r} is an arbitrary position vector. Similarly, the geometrical factors $\{Q_n^\mu\}$ are defined by the quantity $(\mathbf{k} \cdot \mathbf{r})(\boldsymbol{\epsilon} \cdot \mathbf{r})$ appearing in the multipole expansion of the scattering amplitude. Here $n = 1, 2, 3, 4$, and 5 correspond to the quadrupole basis $x^2 - y^2, 3z^2 - r^2, yz, zx$, and xy , respectively. By noticing the fact that $\mathbf{k} = |\mathbf{k}|\mathbf{e}_{z'}$, we define $\{Q_n^\mu\}$ in the following relations.

$$(\mathbf{k} \cdot \mathbf{r})(\boldsymbol{\epsilon}^\sigma \cdot \mathbf{r}) \propto z'_4 = \sum_{n=1}^5 Q_n^\sigma z_n''', \quad (\text{A}\cdot 3)$$

$$(\mathbf{k} \cdot \mathbf{r})(\boldsymbol{\epsilon}^\pi \cdot \mathbf{r}) \propto -z'_3 = \sum_{n=1}^5 Q_n^\sigma z_n''', \quad (\text{A}\cdot 4)$$

where $z_1 = \frac{\sqrt{3}}{2}(x^2 - y^2)$, $z_2 = \frac{1}{2}(3z^2 - r^2)$, $z_3 = \sqrt{3}yz$, $z_4 = \sqrt{3}zx$, and $z_5 = \sqrt{3}xy$.

From eqs. (A.1) ~ (A.4), the geometrical factors are evaluated by expressing x', y' in terms of x''', y''', z''' for the dipole transition and z'_4, z'_3 in terms of z_μ''' for the quadrupole transition, respectively, with the help of rotation matrix. The final results for the σ polarization with the incident photon are as follows:

$$P_x^\sigma = \cos \alpha \cos \beta \cos \psi + \sin \alpha \sin \psi, \quad (\text{A}\cdot 5)$$

$$P_y^\sigma = \sin \alpha \cos \beta \cos \psi - \cos \alpha \sin \psi, \quad (\text{A}\cdot 6)$$

$$P_z^\sigma = -\sin \beta \cos \psi, \quad (\text{A}\cdot 7)$$

$$Q_1^\sigma = \frac{1}{2} \sin \theta (-\cos \psi \cos 2\alpha \sin 2\beta - 2 \sin \psi \sin 2\alpha \sin \beta) \\ + \frac{1}{2} \cos \theta [\sin 2\psi \cos 2\alpha (1 + \cos^2 \beta) - 2 \cos 2\psi \sin 2\alpha \cos \beta], \quad (\text{A}\cdot 8)$$

$$Q_2^\sigma = \frac{\sqrt{3}}{2} \sin \theta \cos \psi \sin 2\beta + \frac{\sqrt{3}}{2} \cos \theta \sin 2\psi \sin^2 \beta, \quad (\text{A}\cdot 9)$$

$$Q_3^\sigma = \sin \theta (-\cos \psi \sin \alpha \cos 2\beta + \sin \psi \cos \alpha \cos \beta) \\ + \frac{1}{2} \cos \theta (-\sin 2\psi \sin \alpha \sin 2\beta - 2 \cos 2\psi \cos \alpha \sin \beta), \quad (\text{A}\cdot 10)$$

$$Q_4^\sigma = \sin \theta (-\cos \psi \cos \alpha \cos 2\beta - \sin \psi \sin \alpha \cos \beta) \\ + \frac{1}{2} \cos \theta (-\sin 2\psi \cos \alpha \sin 2\beta + 2 \cos 2\psi \sin \alpha \sin \beta), \quad (\text{A}\cdot 11)$$

$$Q_5^\sigma = \frac{1}{2} \sin \theta (-\cos \psi \sin 2\alpha \sin 2\beta + 2 \sin \psi \cos 2\alpha \sin \beta) \\ + \frac{1}{2} \cos \theta [\sin 2\psi \sin 2\alpha (1 + \cos^2 \beta) + 2 \cos 2\psi \cos 2\alpha \cos \beta]. \quad (\text{A}\cdot 12)$$

For $(004\ell + 2)$, putting $\alpha = \beta = 0$, we have $P_x^\sigma = \cos \psi$, $P_y^\sigma = -\sin \psi$, $P_z^\sigma = 0$, and $Q_1^\sigma = \sin 2\psi \cos \theta$, $Q_2^\sigma = 0$, $Q_3^\sigma = \sin \psi \sin \theta$, $Q_4^\sigma = -\cos \psi \sin \theta$, $Q_5^\sigma = \cos 2\psi \cos \theta$. For $(\ell\ell\ell)$, putting $\alpha = \pi/4$ and $\beta = \sin^{-1} \sqrt{2/3}$, we have

$$P_x^\sigma = \sqrt{\frac{1}{6}} [\cos \psi + \sqrt{3} \sin \psi], \quad (\text{A}\cdot 13)$$

$$P_y^\sigma = \sqrt{\frac{1}{6}} [\cos \psi - \sqrt{3} \sin \psi], \quad (\text{A}\cdot 14)$$

$$P_z^\sigma = -\sqrt{\frac{2}{3}} \cos \psi, \quad (\text{A}\cdot\text{15})$$

$$Q_1^\sigma = \sqrt{\frac{1}{3}} \left[-\cos 2\psi \cos \theta - \sqrt{2} \sin \psi \sin \theta \right], \quad (\text{A}\cdot\text{16})$$

$$Q_2^\sigma = \sqrt{\frac{1}{3}} \left[\sin 2\psi \cos \theta + \sqrt{2} \cos \psi \sin \theta \right], \quad (\text{A}\cdot\text{17})$$

$$Q_3^\sigma = \frac{1}{3} \sqrt{\frac{1}{2}} \left[-\sqrt{6} \cos 2\psi \cos \theta - \sqrt{2} \sin 2\psi \cos \theta \right. \\ \left. + \cos \psi \sin \theta + \sqrt{3} \sin \psi \sin \theta \right], \quad (\text{A}\cdot\text{18})$$

$$Q_4^\sigma = \frac{1}{3} \sqrt{\frac{1}{2}} \left[\sqrt{6} \cos 2\psi \cos \theta - \sqrt{2} \sin 2\psi \cos \theta \right. \\ \left. + \cos \psi \sin \theta - \sqrt{3} \sin \psi \sin \theta \right], \quad (\text{A}\cdot\text{19})$$

$$Q_5^\sigma = \frac{\sqrt{2}}{3} \left[\sqrt{2} \sin 2\psi \cos \theta - \cos \psi \sin \theta \right]. \quad (\text{A}\cdot\text{20})$$

The expressions for the scattered photon are obtained by replacing θ with $-\theta$ in the above expressions.

References

- 1) J. P. Hill, C.-C. Kao, and D. F. McMorrow: Phys. Rev. B **55** (1997) R8662.
- 2) Y. Murakami, H. Kawada, H. Kawata, M. Tanaka, T. Arima, Y. Moritomo, and Y. Tokura: Phys. Rev. Lett. **80** (1998) 1932.
- 3) Y. Murakami, J. P. Hill, D. Gibbs, M. Blume, I. Koyama, M. Tanaka, H. Kawata, T. Arima, Y. Tokura, K. Hirota, and Y. Endoh: Phys. Rev. Lett. **81** (1998) 582.
- 4) W. Neubeck, C. Vettier, K.-B. Lee, and F. de Bergevin: Phys. Rev. B **60** (1999) R9912.
- 5) S. Grenier, J. P. Hill, D. Gibbs, K. J. Thomas, M. v. Zimmermann, C. S. Nelson, V. Kiryukhin, Y. Tokura, Y. Tomioka, D. Casa, T. Gog, and C. Venkataraman: Phys. Rev. B **69** (2004) 134419.
- 6) I. S. Elfimov, V. I. Anisimov, and G. A. Sawatzky: Phys. Rev. Lett. **82** (1999) 4264.
- 7) M. Benfatto, Y. Joly, and C. R. Natoli: Phys. Rev. Lett. **83** (1999) 636.
- 8) M. Takahashi, J. Igarashi, and P. Fulde: J. Phys. Soc. Jpn. **68** (1999) 2530.
- 9) M. Takahashi, J. Igarashi, and P. Fulde: J. Phys. Soc. Jpn. **69** (2000) 1614.
- 10) D. H. Templeton and L. K. Templeton: Phys. Rev. B **49** (1994) 14850.
- 11) I. S. Elfimov, N. A. Skorikov, V. I. Anisimov, and G. A. Sawatzky: Phys. Rev. Lett. **88** (2002) 015504.
- 12) L. Paolasini, C. Vettier, F. de Bergevin, F. Yakhou, D. Mannix, A. Stunault, W. Neubeck, M. Altarelli, M. Fabrizio, P. A. Metcalf, and J. M. Honig: Phys. Rev. Lett. **82** (1999) 4719.
- 13) A. Tanaka: J. Phys. Soc. Jpn. **71** (2002) 1091.
- 14) Y. Jolly, S. Di Matteo, and C. R. Natoli: Phys. Rev. B **69** (2004) 224401.
- 15) S. W. Lovesey, J. Fernández-Rodríguez, J. A. Blanco, D. S. Sivia, K. S. Knight, and L. Paolasini: Phys. Rev. B **75** (2007) 014409.
- 16) T. Arima, J.-H. Jung, M. Matsubara, M. Kubota, J.-P. He, Y. Kaneko, and Y. Tokura: J. Phys. Soc. Jpn. **74** (2005) 1419.
- 17) S. Di Matteo and Y. Joly: Phys. Rev. B **74** (2006) 014403.
- 18) S. W. Lovesey, K. S. Knight, and E. Balcar: J. Phys.: Condens. **19** (2007) 376205.
- 19) S. Di Matteo, Y. Joly, and C. R. Natoli: Phys. Rev. B **72** (2005) 144406.
- 20) S. P. Collins, S. W. Lovesey, and E. Balcar: J. Phys.: Condens. **19** (2007) 213201.
- 21) J. García, G. Subías, M. G. Proietti, J. Blasco, H. Renevier, J. L. Hodeau, and Y. Joly: Phys. Rev. B **63** (2001) 054110.
- 22) M. Kanazawa, K. Hagiwara, J. Kokubun, and K. Ishida: J. Phys. Soc. Jpn. **71** (2002) 1765.
- 23) H. Kawata and K. Mori: Rev. Sci. Instrum. **66** (1995) 1407.
- 24) M. Matsubara, Y. Shimada, T. Arima, Y. Taguchi, and Y. Tokura: Phys. Rev. B **72** (2005) 220404(R).
- 25) P. W. Anderson: Phys. Rev. **124** (1961) 41.
- 26) It is known that the thermal lattice vibration around the center of tetrahedrons could cause the intensities around the main K-edge region through the $E1$ - $E1$ process. See, for such analysis, V. E. Dmitrienko and E. N. Ovchinnikova: Acta Crystallogr., Sect. A **56** (2000) 340.
- 27) M. Matsubara: Dr. Thesis, Faculty of Engineering, University of Tokyo, Tokyo (2005).
- 28) E. J. W. Verway: Nature **144** (1939) 327.
- 29) I. Leonov, A. N. Yaresko, V. N. Antonov, and V. I. Anisimov: Phys. Rev. B **74** (2006) 165117.
- 30) E. Nazarenko, J. E. Lorenzo, Y. Joly, J. L. Hodeau, D. Mannix, and C. Marin: Phys. Rev. Lett.

- 97** (2006) 056403 [Errata; **98** (2007) 089902].
- 31) H. Uzu and A. Tanaka: J. Phys. Soc. Jpn. **75** (2006) 043704.
- 32) R. Cowan: *The Theory of Atomic Structure and Spectra* (University of California Press, Berkeley, 1981).
- 33) F. M. F. de Groot, J. C. Fuggle, B. T. Thole, and G. A. Sawatzky: Phys. Rev. B **42** (1990) 5459.
- 34) J. Chen, D. J. Huang, A. Tanaka, C. F. Chang, S. C. Chung, W. B. Wu, and C. T. Chen: Phys. Rev. B **69** (2004) 085107.
- 35) For NiO, see M. Usuda, M. Takahashi, and J. Igarashi: Phys. Rev. B **69** (2004) 014408.
- 36) K. Matsumoto, F. Saito, T. Toda, K. Ohkubo, K. Yamawaki, T. Mori, K. Hirano, M Tanaka, and S. Sasaki: Jpn. J. Appl. Phys. **39** (2000) 6089.
- 37) In many literatures, the scattering vector is defined by $\mathbf{G} = \mathbf{k} - \mathbf{k}'$, which is different from our definition $\mathbf{G} = \mathbf{k}' - \mathbf{k}$. The difference in definition is discernible for systems without centrosymmetry.
- 38) P. J. Brown, A. G. Fox, J. I. Langford, H. Lipson, E. N. Maslen, M. A. O'Keefe, T. M. Sabine, and B. T. M. Willis: in *International Tables for Crystallography*, eds. A. J. C. Willson and E. Prince (Kluwer Academic, Boston, 1999) 2nd ed., Vol. C, Chap. 6, p.547.
- 39) M. E. Rose: *Elementary Theory of Angular Momentum* (John Wiley and Sons, Inc., New York, 1957).